

Beyond-mean-field-model analysis of low-spin normal-deformed and superdeformed collective states of ^{32}S , ^{36}Ar , ^{38}Ar and ^{40}Ca

M. Bender,¹ H. Flocard,² and P.-H. Heenen¹

¹Service de Physique Nucléaire Théorique, Université Libre de Bruxelles, C.P. 229, B-1050 Bruxelles, Belgium

²CSNSM, Bt.104, F-91405 Orsay Campus, France

(Dated: May 8, 2003)

We investigate the coexistence of spherical, deformed and superdeformed states at low spin in ^{32}S , ^{36}Ar , ^{38}Ar and ^{40}Ca . The microscopic states are constructed by configuration mixing of BCS states projected on good particle number and angular momentum. The BCS states are themselves obtained from Hartree-Fock BCS calculations using the Skyrme interaction SLy6 for the particle-hole channel, and a density-dependent contact force in the pairing channel. The same interaction is used within the Generator Coordinate Method to determine the configuration mixing and calculate the properties of even-spin states with positive parity. Our calculations underestimate moments of inertia. Nevertheless, for the four nuclei, the global structural properties of the states of normal deformation as well as the recently discovered superdeformed bands up to spin 6 are correctly reproduced with regard to both the energies and the transition rates.

PACS numbers: 21.10.Ky, 21.10.Re, 21.30.Fe, 21.60.Jz, 27.30.+t

I. INTRODUCTION

The existence of deformed bands in the spectrum of nuclei whose ground state is spherical has been established since the sixties for ^{16}O , and since the early 1970s for ^{40}Ca [1]. With the modern large multi-detector γ arrays like Euroball and Gammasphere, many more normal-deformed and even superdeformed rotational bands have been uncovered in these systems, such as those explored up to very high spin in doubly-magic ^{40}Ca [2, 3], and the adjacent transitional nuclei ^{36}Ar [4, 5] and ^{38}Ar [6]. The occurrence of well-deformed prolate structures in such magic or close-to-magic nuclei is understood as resulting from a drastic reorganization of the Fermi sea in which the oblate deformation driving last level of the shells are emptied while orbitals originating from the $f_{7/2}$ shell are filled.

On the theoretical side, the new structures have been explored with the cranked mean-field (MF) method [2] in which such a reorganization is naturally taken into account. On the other hand, thanks to conceptual and numerical progress that took place over the last decade, the shell model method is now also in position to analyze spectra in which spherical and well-deformed configurations coexist. However, in the latter case, the complexity of the calculation often prevents full scale diagonalizations in complete shells and specific choices must be made for the extension of the basis in order to keep computations within reach of present technology. In some sense, prior to the diagonalization, the expected physics is introduced in the Hamiltonian to use. This choice is vindicated by the outcome of calculations and superdeformed bands built on particle excitations to the pf shells do come out. The cranked MF method does not have to make such an *a priori* choice; if a reorganization of the Fermi sea is required, it will occur naturally as a consequence of energy optimization. The present work

illustrates a class of methods attempting to bridge the gap between these two approaches while remaining close to the MF in spirit. Indeed, the introduction of a diagonalization within a class of MF collective states and the restoration of symmetries (particle number, angular momentum) broken at the mean-field level transfers the physical description from the intrinsic to the laboratory frame where the shell model naturally operates.

In the next section, we provide a quick overview of the qualitative features of our method, which is described in more detail in [7]. The necessary formalism and notations are also introduced. In the third section, we present our results for the four nuclei ^{40}Ca , ^{38}Ar , ^{36}Ar and ^{32}S ; a selection which keeps in touch with recent experimental progress. Moreover, taking into account an earlier work on ^{16}O [8], this choice allows us to test our method on a set of nuclei illustrating most of the spectroscopic diversity of the sd shell region of the nuclear chart. In this section, our results are compared with data and with those provided by shell model, cranked MF, or other extended-MF calculations.

II. THE METHOD

A. Effective Hamiltonian and Collective Hilbert Space

The N -body physical states analyzed in this work are contained in the Hilbert space spanned by solutions $|\beta_2\rangle$ of Constrained Hartree-Fock-BCS (CHFBCS) equations [9]. In those equations, the constraint is imposed on the axial mass quadrupole moment operator \hat{Q}_{20} . The notation β_2 is a label standing for any quantity in one to one correspondance with the expectation value $Q_2 = \langle \beta_2 | \hat{Q}_{20} | \beta_2 \rangle$. The single-particle wave functions from which BCS states are constructed are discretized on a three-dimensional mesh. As explained in

Ref. [10], this technique provides accurate solutions of the mean-field equations. Note that our calculation does not assume the existence of an inert core.

As two-body interaction in the particle-hole channel of the Hamiltonian \hat{H} , we have chosen the SLy6 parametrization [11] of the Skyrme force. Most of our previous studies were performed with the SLy4 parametrization. Both sets have been fitted on the same set of observables, but differ by the way the center-of-mass motion is treated. In SLy4, only the diagonal part of the cm energy is subtracted from the total energy, while in SLy6, the full cm energy is extracted self-consistently. This difference makes the calculations with SLy6 more time consuming. The cm operator affects also the surface tension of the Skyrme interaction and, in this respect, the SLy6 parametrization seems to be more satisfactory [12]. This better surface tension is the motivation for the choice of SLy6 in the present study. The pairing force is a zero-range, density-dependent force acting predominantly at the surface of the nucleus in order to describe the pairing effects in the particle-particle $T = 1$, $T_z = \pm 1$ channel. The parameters of the latter force [13] are identical for neutrons and protons and taken without readjustment from Refs. [7, 8]. As in earlier calculations, for each nucleon species, the active pairing space is limited to an interval of 10 MeV centered at the Fermi surface. The present study does not therefore involve the definition of a new set of forces. It relies on well established interactions tested within the mean-field approach over a wide range of nuclei and phenomena covering the nuclear chart. This work is thus part of a program whose aim it is to perform an additional evaluation of this Hamiltonian by taking into account the effects of quadrupole correlations.

For the sake of an easier comparison with the literature on quadrupole collective spectroscopy, we adopt the sharp edge liquid drop relation to relate the β_2 deformation parameter and the axial quadrupole moment Q_2

$$\beta_2 = \sqrt{\frac{5}{16\pi}} \frac{4\pi Q_2}{3R^2 A} , \quad (1)$$

where the nuclear radius R in fm at zero deformation is related to its mass A according to the standard formula $R = 1.2 A^{1/3}$. In this paper, only axial prolate and oblate deformations are considered. As we are mostly concerned with low-energy collective spectroscopy, we consider a range of values of β_2 covering all deformations such that the excitation energy of the constrained BCS states with respect to that of the spherical configuration $|\beta_2 = 0\rangle$ is at most 20 MeV.

In the CHFBCS equations, we also introduce the correction terms associated with the Lipkin-Nogami prescription (see Ref. [9] for a description and for further references). Indeed, within schematic models, these terms have been shown to make the BCS solutions closer to those which would result from a full variation after projection on the particle number. Thus, they should be appropriate for calculations such as ours where a projec-

tion on N and Z is anyhow carried out at a later stage. Another benefit of the LN method is that it suppresses the collapse of pairing correlations which may otherwise occurs when the density of single-particle states around the Fermi level is small. It therefore ensures a smooth behavior as a function of the quadrupole moment of the overlap and energy kernels which intervene in the Generator Coordinate Method (GCM).

Several fundamental symmetries are broken in the BCS states $|\beta_2\rangle$, which are eigenstates neither of the particle numbers nor of the angular momentum.¹ We restore these symmetries by means of a triple projection: first on the proton and neutron numbers Z and N , then on the total spin J . For a given nucleus, the BCS state $|\beta_2\rangle$ has been determined with the usual constraints ensuring that the expectation values of the proton and neutron numbers have the correct Z and N values. In the following, we only select that component of the BCS state $|\beta_2\rangle$ which is an eigenstate of the particle number operators for the same values, discarding the $Z \pm 2, 4, \dots$ and $N \pm 2, 4, \dots$ components. For this reason, we do not introduce particle number labels and use the notation $|\beta_2\rangle$ for the particle-number projected state.

By contrast, the CHFBCS equations leading to the states $|\beta_2\rangle$ do not include any constraint on the angular momentum expectation value. Starting from the N and Z projected states, we will consider separately all the collective Hilbert spaces spanned by the components $|J\beta_2\rangle$ resulting from a projection of the $|\beta_2\rangle$'s on the subspace of the even total angular momentum J . Hereafter, the notation $|J, \beta_2\rangle$ stands for any of the states associated with the $2J + 1$ values of the the third component of the angular momentum. Note that, because the initial CHFBCS equations do not break the reflection or the time-reversal symmetry, the model provides no information on odd-spin states.

Finally, we diagonalize the Hamiltonian \hat{H} within each of the collective subspaces of the non-orthogonal bases $|J, \beta_2\rangle$ by means of the Generator Coordinate Method (GCM) [9, 14, 15]. This leads to a set of orthogonal collective states $|J, k\rangle$ where k is a discrete index which labels spin J states according to increasing energy. As for $|J, \beta_2\rangle$ the notation $|J, k\rangle$ stands for any state of the spin multiplet. A byproduct of the GCM are the collective wave functions $g_{J,k}(\beta_2)$ describing the distribution of the states $|J, k\rangle$ over the family $|J, \beta_2\rangle$. All collective properties discussed hereafter are directly computed from the N -body physical states $|J, k\rangle$.

We stress that the correlations introduced by the different configuration mixings of the initial mean-field wave functions $|\beta_2\rangle$ achieve several goals. First, the particle-number projection corrects a deficiency of the BCS description of pairing in finite systems. Second, the an-

¹ Among others that we do not discuss are translational, and isospin invariance.

angular momentum projection separates the dynamics according to spin and allows a direct calculation of electromagnetic moments and transition probabilities in the laboratory rather than the intrinsic frame. Finally, performing a configuration mixing over the coordinate β_2 by the GCM, we construct a set of orthonormal states $|J, k\rangle$ in which the large-amplitude quadrupole collective correlations are taken into account.

B. Charge multipole and transition moments

The angular-momentum projection performs a transformation to the laboratory frame of reference and, therefore, an intrinsic deformation cannot be unambiguously assigned to the projected states $|J, k\rangle$. For instance, all states $|0, k\rangle$ have a quadrupole moment equal to zero. On the other hand, any multipole operator can be calculated in a straightforward, although sometimes tedious, manner directly from matrix elements involving the BCS states $|\beta_2\rangle$.

It is, however useful to extract quantities analogous to intrinsic frame quantities from physically well-defined observables such as spectroscopic or transition moments, in order to achieve contact with standard mean-field approaches. For instance, when transition probabilities suggest that the two states $|J_i, k\rangle$ and $|J_f, k\rangle$ can be interpreted as forming a rotational band, one can define a charge intrinsic moment $Q_{c2}^{(t)}(J, k)$ (c stands for “charge” and t for “transition”) from the $B(E2, J_i \rightarrow J_f)$ according to the standard formulas [16]. Our model relies on the mixing of purely axial quadrupole deformed configurations and describes $K = 0$ positive parity bands only. Moreover, since the CHFBCS equations do not include a spin cranking term, the quality of the description of $|J, k\rangle$ states will deteriorate with spin J . In the following, we will consider only spins up to 10. A first possible definition of the intrinsic quadrupole moment $Q_{c2}^{(t)}(J, k)$ is thus:

$$Q_{c2}^{(t)}(J, k) = \sqrt{\frac{16\pi}{5} \frac{B(E2, J \rightarrow J-2)}{\langle J020|J-20\rangle^2 e^2}}, \quad (2)$$

whith the notation of Ref. [17] for Clebsch-Gordan coefficients. Within the rigid rotor model, one can also define an intrinsic quadrupole moment $Q_{c2}^{(s)}(J, k)$ (s stands here for “spectroscopic”) of a state with spin J ($J \neq 0$) related with the spectroscopic quadrupole moment

$$Q_c(J, k) = \langle J, k | \hat{Q}_{c22} | J, k \rangle, \quad (3)$$

in the laboratory frame, via the relation

$$Q_{c2}^{(s)}(J, k) = -\frac{2J+3}{J} Q_c(J, k). \quad (4)$$

In Eq. (3), it is understood that the bra and kets both correspond to the $M = J$ component of the $2J+1$ multiplet. The values of $Q_{c2}^{(s)}(J, k)$ and $Q_{c2}^{(t)}(J, k)$ are equal

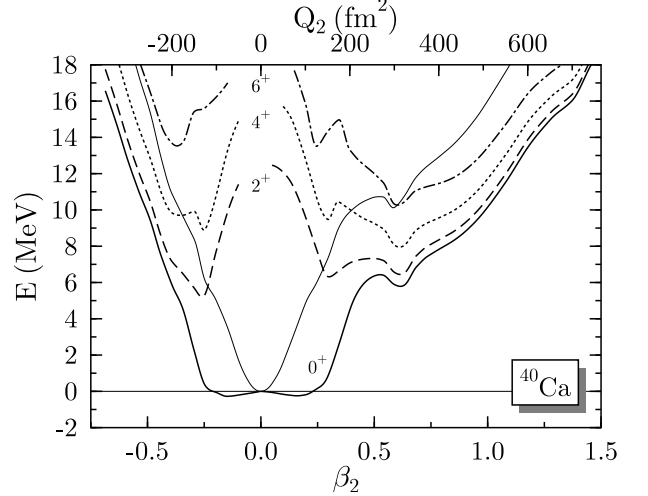


FIG. 1: Nucleus ^{40}Ca ; Projected energy curves versus the mass deformation (β_2 and Q_2). The thin solid curve gives $\langle \beta_2 | \hat{H} | \beta_2 \rangle$ (MF), while the thick solid, dashed, dotted and dash-dotted curves correspond to $\langle J, \beta_2 | \hat{H} | J, \beta_2 \rangle$ (PMF) for the values $J = 0, 2, 4$ and 6 respectively. The energy origin is taken at $\langle \beta_2 = 0 | \hat{H} | \beta_2 = 0 \rangle$.

when the rigid rotor assumption is strictly fulfilled. The differences between the values of these two quantities will tell us how well this assumption is satisfied by the calculated physical states. Instead of $Q_{c2}^{(s)}(J, k)$ and $Q_{c2}^{(t)}(J, k)$, we will equivalently consider the dimensionless quantities $\beta_{c2}^{(s)}(J, k)$ and $\beta_{c2}^{(t)}(J, k)$ calculated according to a relation similar to Eq. (1) in which the mass A is replaced by the number of protons Z since we are dealing with the charge quadrupole moment.

Technical details on the evaluation of $Q_c(J, k)$ and $B(E2)$ will be given in an appendix below.

III. RESULTS

A. ^{40}Ca

The ground state of the $N = Z$ doubly-magic nucleus ^{40}Ca is spherical. As in several magic nuclei, the lowest excited state is a 3^- state at 3.74 MeV. This state as well as other negative parity states is not included in the Hilbert space of our calculation. Its study requires parity breaking mean-field calculation involving octupole deformations as done in a previous study performed for Pb isotopes [18].

The lowest states of several even parity rotational bands are known since the early 70’s [1]. More recently, several normal- and also superdeformed bands have been identified up to very high spin thanks in particular, to a recent Gammasphere+Microball experiment [2].

In Fig. 1, we have plotted the particle projected mean-field deformation energy curve (denoted below

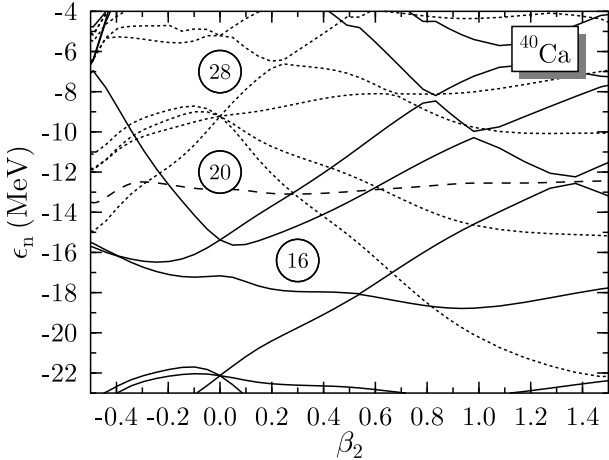


FIG. 2: Nucleus ^{40}Ca ; Self-Consistent HFBCS Nilsson diagram for neutrons. Except for an overall Coulomb shift, the proton spectrum is almost identical. The dashed curve gives the Fermi energy.

as MF) $\langle \beta_2 | \hat{H} | \beta_2 \rangle$ and the particle number and spin-projected mean-field curves $\langle J, \beta_2 | \hat{H} | J, \beta_2 \rangle$ (denoted below as PMF) for low spin values. In addition to the expected well marked spherical minimum, the MF curve displays a superdeformed secondary minimum around $\beta_2 = 0.5$. The $J = 0$ PMF curve is almost flat over the range $-0.2 \leq \beta_2 \leq 0.2$. It also presents a secondary minimum around $\beta_2 = 0.5$. The minima of the higher spin PMF curves correspond to both oblate and prolate deformations at $\beta_2 \approx \pm 0.2$ and to the prolate superdeformation $\beta_2 = 0.5$. This latter minimum becomes the lowest one from spin 4 upward. These features of the mean-field curves are consistent with the HFBCS self-consistent single-particle diagram shown in Fig. 2, where a small gap is visible at $\beta_2 = 0.4$. At $\beta_2 = 0.6$, a prolate deformation-driving orbital, originating from the $f_{7/2}$ shell, is occupied, creating a deformed shell gap. Note that the deformed gap at $\beta_2 = 0.9$ shows up as a softening of the MF and PMF curves.

In Fig. 3, along with the MF and PMF curves, we show the excitation energies

$$E_{J,k} = \langle J, k | \hat{H} | J, k \rangle \quad (5)$$

of the GCM states for the spins $J = 0, 2, 4$ and 6 . From the GCM collective wave-function $g_{J,k}$ of each state $|J, k\rangle$, a mean deformation can be calculated

$$\bar{\beta}_2 = \int \beta_2 g_{J,k}(\beta_2)^2 d\beta_2. \quad (6)$$

This quantity does not necessarily coincide with the deformation $\beta_{c2}^{(s)}(J, k)$ calculated from Eqs. (3) of (4), but provides a convenient indicator of the weight of deformed mean-field states in the projected state. It can be different from zero for $J = 0$ for which $\beta_{c2}^{(s)}(J, k)$ vanishes. In particular, it allows one to detect the 0^+ band head

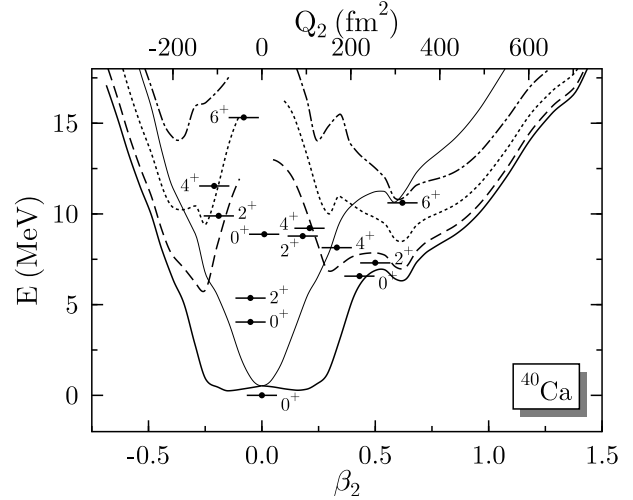


FIG. 3: Nucleus ^{40}Ca ; MF $\langle \beta_2 | \hat{H} | \beta_2 \rangle$ (thin solid) and PMF $\langle J, \beta_2 | \hat{H} | J, \beta_2 \rangle$ (thick solid) deformation energy curves. The ordinates of short horizontal segments give the energy $E_{J,k}$ of the GCM states (Eq. 5). The abscissae of the black points indicate the mean deformation ($\bar{\beta}_2$) of the corresponding collective wave-function $g_{J,k}$ (Eq. 6). The energy origin is taken at $E_{0,1}$.

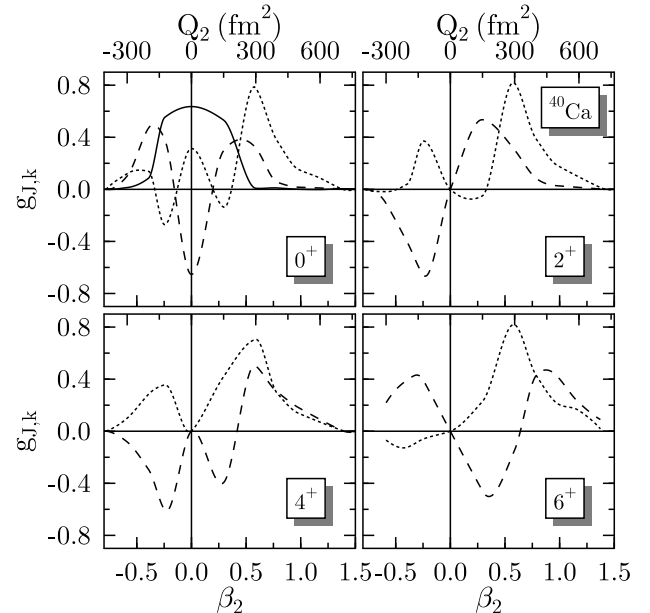


FIG. 4: Collective GCM wave-functions $g_{J,k}$ for low-spin states of ^{40}Ca . The ground-state 0^+ wave function is drawn with a thick solid line. The wave functions of the ND and SD bands are drawn with dashed and dotted lines respectively.

of a deformed band and to perform a band classification of the states pending confirmation from the analysis of the in-band transitions. The magnitude of the axial quadrupole collective correlations is given by the difference between the energies of the spherical configuration and of the GCM ground state, $E(0, 1)$. It is equal to

TABLE I: Energy, spectroscopic moment and transition amplitudes of some of the ND (upper part) and SD (lower part) bands of ^{40}Ca . The k labeling of the state refers to our calculation. The columns five to eight give the intrinsic moments, see Sect. II B. The last column gives the excitation energy of the most likely corresponding experimental state [2].

GCM State J_k^+	$E_{J,k}$	Q_c	$B(E2) \downarrow$	$Q_{c2}^{(s)}$	$\beta_{c2}^{(s)}$	$Q_{c2}^{(t)}$	$\beta_{c2}^{(t)}$	E_{exp} (MeV)
	(MeV)	($e \text{ fm}^2$)	($e^2 \text{ fm}^4$)	($e \text{ fm}^2$)		($e \text{ fm}^2$)		
0_2^+	3.99	0.0	—	—	—	—	—	3.35
2_1^+	5.40	2.2	112	-7.8	-0.031	75.2	0.30	3.91
4_2^+	9.28	-18.7	16	51.3	0.201	23.9	0.09	5.28
6_2^+	13.39	-34.3	187	85.8	0.336	77.4	0.26	6.93
0_3^+	6.52	0.0	—	—	—	—	—	5.21
2_2^+	7.30	-38.2	447	133.9	0.525	150	0.60	5.63
4_1^+	8.15	-35.5	373	97.6	0.383	115	0.44	6.54
6_1^+	10.53	-64.1	557	160.2	0.628	133	0.51	7.97
8_1^+	13.07	-66.5	882	157.9	0.619	163	0.64	9.856
10_1^+	16.18	-70.1	962	161.2	0.63	169	0.66	12.338

0.526 MeV, a value consistent with estimates in other nuclei [18]. Among the many J_k^+ GCM states, one observes at large deformation, $\bar{\beta}_2 \approx 0.5$, a subset ($0_3, 2_2, 4_1, 6_1$) whose members can plausibly be assigned to a superdeformed band (SD). This band is interpreted within the shell model as a 8p-8h band. The other excited states have smaller $\bar{\beta}_2$ values. At lower excitation energy, we will analyze whether the states ($0_2, 2_1, 4_2, 6_2$) can be interpreted as the observed normal deformed (ND) band.

In Fig. 4, we have plotted the collective wave functions $g_{J,k}$. The position of their nodes can only be understood if one keeps in mind the fact that, because the exchanges of intrinsic axes are included in a three-dimensional rotation, the quadrupole dynamics is not undimensional. It takes place in the full quadrupole β_2, γ plane along the six lines associated with the gamma angles $\gamma_j = 2j\pi/6$, $j = 0, \dots, 5$ [19]. The underlying group structure also imposes that all non-zero- J collective wave-functions vanish at $\beta_2 = 0$.

Fig. 5 compares the calculated and experimental excitation energies of the low spin states. The GCM states (right-hand side) can be assigned to ND or SD bands according to their $\bar{\beta}_2$ value. On the left side, we have drawn the experimental states to which these bands most likely correspond. In addition, at the extreme left side of the picture, we have plotted two other states observed within the same range of spins and excitation energies (2^+ at 5.249 MeV and 4^+ at 6.509 MeV). However, we feel entitled to eliminate them from our discussion of the GCM results because, according to some theoretical models [20], they correspond to a $K = 2$ band which, cannot be described within the present purely axial model.

The upper part of Table I collects data for the states of the ND band (labelled “band 2” in [2]). They have already been analyzed by Nathan *et al.* [1] in the early 70s in terms of a 4p-4h structure.

The GCM bandheads are at about the right excitation energy. However, the overall spectrum is too spread out. Since this is a general trend of this calculation, we defer a discussion of possible causes to the conclusions section. On the other hand, the $B(E2)$ values, or equivalently the $Q_{c2}^{(t)}(J, k)$ moments, of the $E2$ transitions originating from the 2_1^+ and the 6_2^+ are in nice agreement with the experimental value $Q_{c2}^{(t)}(J, k) = 74 \pm 14 \text{ e fm}^2$ [2]. In our calculation, the transition down from the 4_2^+ is reduced due to a coupling with the 4_1^+ state of the SD band. This coupling is probably a spurious consequence of the too large spreading of the GCM ND band which pushes the ND 4^+ level in the vicinity of the SD 4^+ state. Another consequence of the ND band spreading is that the SD 4^+ and 6^+ states are the lowest ones, while experiment suggests that this band is not yrast below the highest observed spin ($J = 16$). Our calculated value for the monopole transition matrix element $|M(E0)| = 1.3 \text{ e fm}^2$ is smaller, but of the same order of magnitude as the

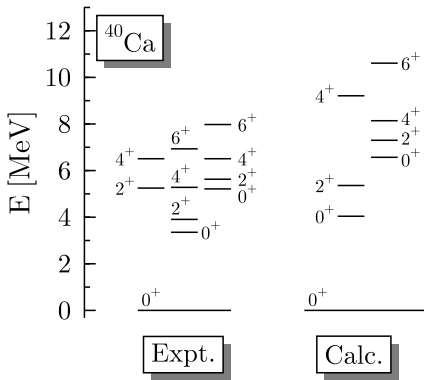


FIG. 5: Comparison of experimental (left) and calculated (right) excitation spectrum of even spin and positive parity states in ^{40}Ca .

experimental value $(2.6 \pm 0.1) e \text{ fm}^2$ [21]. Note that no effective charge is used in our calculation.

In the MF curve, the barrier between normal deformations and the SD minimum does not exceed 0.5 MeV as seen in Fig. 1. The excitation energy of this SD minimum is 10.1 MeV, a value much larger than the value of 5.213 MeV observed for the SD bandhead (band 1 in [2]). Angular-momentum projection reduces this excitation energy to 6.1 MeV. Finally, the quadrupole correlations due to configuration-mixing push the excitation energy of the SD bandhead to 6.52 MeV. As seen in Fig. 3, this small increase is related to the contribution of quadrupole correlations to the energy, which is larger for the 0_1^+ ground state than for the 0_3^+ state. Thus, although the GCM result shows a significant improvement with respect to MF ones, the final outcome is not as satisfactory in ^{40}Ca as it is in ^{16}O [8], where a better agreement with experiment had been found.

The GCM states $(0_3^+, 2_2^+, 4_1^+, 6_1^+)$ form a SD band with an average deformation $\beta_2 = 0.5$. Their properties are given in the lower part of Table II. As compared with experiment, see Fig. 3, the bandhead is slightly too high in excitation energy and the moment of inertia too small. Still, the agreement is much better than for the ND band. One notes an irregularity for the 4^+ state, due to the already mentioned mixing with a nearby ND state. The calculated transition quadrupole moments for the various transitions in the SD band are in good agreement with the experimental value $Q_{c2}^{(t)} = 180^{+39}_{-29} e \text{ fm}^2$ given in Ref. [2], especially if one takes into account that in our calculation the $6_1^+ \rightarrow 4_1^+$ and $4_1^+ \rightarrow 2_2^+$ transition rates are decreased by a mixing of the 4_2^+ level with the less deformed 4_1^+ state. The proximity of the values of $Q_{c2}^{(t)}$ and $Q_{c2}^{(s)}$ shows also that the SD band satisfies the rotor criterion.

A more recent analysis of transition quadrupole moments within the SD band presented in Ref. [3] suggests that $Q_{c2}^{(t)}$ drops from values around $180 e \text{ fm}^2$ at high spin to values around $120 e \text{ fm}^2$ for the $6^+ \rightarrow 4^+$ transition. Our calculation is in agreement with this finding, although it predicts the change a few units of angular momentum too low.

Particle-hole analysis of the GCM states

The ND and SD bands are often interpreted in terms of 4p-4h and 8p-8h configurations respectively. This is for instance the case in RMF calculations without pairing performed with the NL3 parametrization by the Lund group [4]. Similarly, a shell model calculation by Caurier *et al.* [22] in a restricted model space assigns the ND and SD bands to 4p-4h and 8p-8h configurations, respectively. It also finds that calculated transition probabilities related to quadrupole moments cluster around $Q_{c2}^{(t)} = 170 e \text{ fm}^2$, and are slightly decreasing with angular momentum. It, thus, seemed of interest to perform a similar

TABLE II: Properties of the self-consistent np - nh HF states and overlap with low-lying 0^+ GCM states. The second and third columns give the excitation energy with respect to that of the (0p-0h) HF ground state of the HF states (E_{np-nh}) and of its $J = 0$ component ($E_{J=0np-nh}$). The next two columns give the the HF Intrinsic quadrupole moment Q_2 and the associated deformation β_2 . The last three columns give the squared overlaps $|\langle J = 0k | np-nh \rangle|^2$ with the lowest $|J = 0, k\rangle$ GCM states. The normalization of the particle-hole states $|np-nh\rangle$ is chosen such that the norm of its $J = 0$ component is equal to 1.

state	E_{HF} (MeV)	$E_{J\text{HF}}$ (MeV)	Q_2 (fm 2)	β_2	$ \langle Jk J\text{HF} \rangle ^2$		
					0_1^+	0_2^+	0_3^+
0p-0h	0.002	0.000	0	0.000	0.6163	0.2170	0.0363
2p-2h(p)	11.151	8.896	73	0.143	0.1189	0.0413	0.0330
2p-2h(n)	11.462	9.071	73	0.143	0.1083	0.0421	0.0317
4p-4h	11.767	8.729	211	0.414	0.0107	0.1131	0.0938
6p-6h(p)	15.586	11.846	297	0.582	0.0000	0.0124	0.1626
6p-6h(n)	15.791	12.002	298	0.584	0.0000	0.0110	0.1495
8p-8h	13.247	8.732	396	0.777	0.0000	0.0043	0.1378
12p-12h	31.625	26.565	667	1.308	0.0000	0.0000	0.0000

analysis of our results.

The definition of a particle-hole excitation is far from unambiguous. For instance, in the shell model, it is defined with respect to the spherical oscillator basis used in the calculation. However carefully this basis is chosen, it remains a technical rather than a physical reference. In keeping with the spirit of a mean-field method, we have defined the np - nh states, $|np-nh\rangle$, by requiring that, for each particle-hole configuration, they minimize

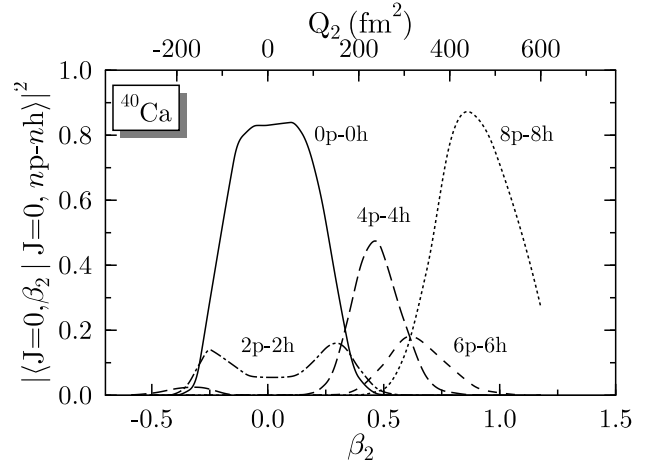


FIG. 6: Square of the overlap $\langle J = 0, \beta_2 | np-nh \rangle$ between the HF $|np-nh\rangle$ states ($n = 0, 2, 4, 6, 8$) and the particle and spin $J = 0$ projected mean-field states $|0, \beta_2\rangle$. Because the two 2p-2h and the 6p-6h overlaps are very similar, only one for each is shown. The normalization of a particle-hole state $|np-nh\rangle$ is chosen so that the norm of its $J = 0$ component is equal to 1.

the Hartree-Fock energy with the same Skyrme Hamiltonian used in the projected GCM study. A deformed state $|np-nh\rangle$, thus, differs from a particle-hole configuration built directly by a simple redefinition of the orbital occupations in the spherical HF ground state $|0p-0h\rangle$. Since the definition of $|np-nh\rangle$ does not involve the pairing channel, all such states are Slater determinants and have the right particle number. In this way, we construct one state for $0p-0h$, $4p-4h$ and $8p-8h$ configurations and two states for $2p-2h$ and $6p-6h$ ones. Because of the self-consistent redefinition of the orbitals, these states are not orthogonal to each other. Although their structure is very different, it turns out that the energy of the spin $J = 0$ component extracted from the $2p-2h$, $4p-4h$, and $8p-8h$ states are almost degenerate, as can be seen in Table II. They are also very excited with respect to both the experimental and the GCM bandheads. There is no obvious explanation for this near-degeneracy, which was already noticed by Zheng *et al.* [23] in a much more schematic mean-field model.

The overlap between the particle-hole states and the $J = 0$ PMF states $|J = 0, \beta_2\rangle$ is plotted in Fig. 6 as a function of β_2 . The overlap for the $|0p-0h\rangle$ is constant over the range $-0.2 \leq \beta_2 \leq 0.2$. This range corresponds to a nearly constant PMF energy, as seen in Fig. 1. The $2p-2h$ overlap is small and vanishes outside this range. The $4p-4h$ overlap is gaussian shaped and peaked at $\beta_2 = 0.5$. The $8p-8h$ curve is peaked at an even larger deformation of $\beta_2 = 0.9$ and its maximum reaches a rather large value (≈ 0.8) indicating that the $J = 0$ component of the $8p-8h$ state is very close to the $|J = 0, \beta_2 = 0.9\rangle$ PMF solutions. All these different deformations are consistent with the locations of deformed shell gaps observed in Fig. 2. On the other hand, the overlap of the $8p-8h$ state is almost zero at the deformation $\beta_2 \approx 0.5$ of the GCM SD band.

These results are already an indication that an analysis in terms of pure particle-hole excitations can only provide a crude approximation. Another indication is that the energies of the $|np-nh\rangle$ states are several MeV larger than those of the $|J = 0, \beta_2\rangle$ states (Table I). This is confirmed by the overlaps given in the last three columns of Table II. It is seen that, with the exception of the GCM ground state 0_1^+ , which, as expected, has a large overlap with the spherical $|0p-0h\rangle$, neither the $4p-4h$ nor the $8p-8h$ HF solutions can be convincingly assigned to the ND or SD GCM bandheads. This is in line with findings of an earlier study of the light doubly-magic nucleus ^{16}O [8].

B. ^{38}Ar

With the same techniques, we analyze three other nuclei, penetrating each time somewhat deeper into the sd shell. As for ^{40}Ca , a recent experiment [6] has found high-spin states of ^{38}Ar which can be interpreted in terms of bands, one of them corresponding to large deformation. In both nuclei, the 0^+ bandheads have not yet

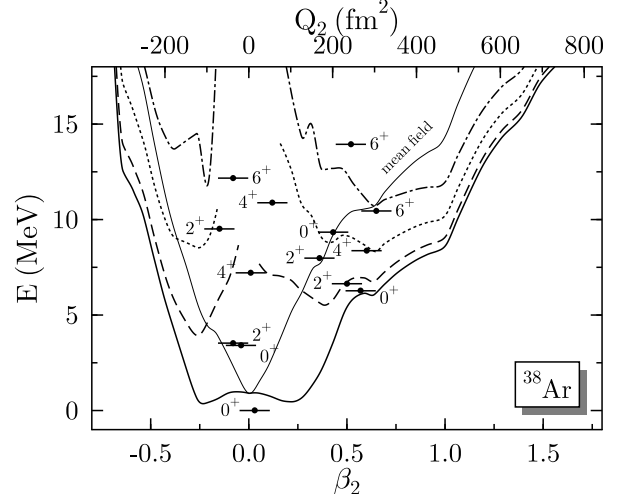


FIG. 7: Nucleus ^{38}Ar ; Deformation energy curves $\langle \beta_2 | \hat{H} | \beta_2 \rangle$ (thin solid line) and $\langle J, \beta_2 | \hat{H} | J, \beta_2 \rangle$ with $J = 0, 2, 4$ and 6 corresponding to thick solid, dashed, dotted and dash-dotted lines, respectively. The ordinates of the short horizontal segments give the energy $E_{J,k}$ (Eq. 5) of the GCM states. The abscissa of the black points indicates the mean deformation $\bar{\beta}_2$ (Eq. 6) of the GCM collective wave-function $g_{J,k}$. The energy origin is taken at $E_{0,1}$.

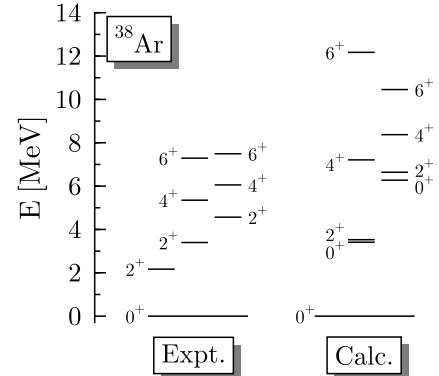


FIG. 8: Same as Fig. 5 for the nucleus ^{38}Ar

been seen. A shell-model analysis has also been done in Ref. [6] within a restricted Hilbert space, as a full $s-d$, $f-p$ shell model calculation is presently beyond computational limits. Nevertheless, the overall quality of the agreement constitutes strong evidence of the importance of $f-p$ excitations. Since the ^{40}Ca subsection has shown that the real underlying structure is likely to be more complex than a single pure $mp-nh$ excitation, it is worth noting that our model has the ability to describe coherent multiple excitation to higher shells.

Keeping in mind the limitations of the present calculation, we concentrate our analysis on the lower part of collective, even parity bands which, in Ref. [6], are labeled 1 and 2, respectively. For instance, our collective space does not include two-quasiparticle configurations and misses the lowest 2^+ state which is well understood

TABLE III: Energy, spectroscopic moment and transitions amplitudes of some of the ND band (upper part) and the SD band(lower part) GCM states of ^{38}Ar . The k labeling of the state refers to our calculation. The columns five to eight give the intrinsic moments (see Sect. II B). The last column gives the experimental excitation energy of the most likely state assignment [6].

GCM state J_k^+	$E_{J,k}$	Q_c	$B(E2) \downarrow$	$Q_{c2}^{(s)}$	$\beta_{c2}^{(s)}$	$Q_{c2}^{(t)}$	$\beta_{c2}^{(t)}$	E_{exp} (MeV)
	(MeV)	($e \text{ fm}^2$)	($e^2 \text{ fm}^4$)	($e \text{ fm}^2$)		($e \text{ fm}^2$)		
0_2^+	3.44	0.0	—	—	—	—	—	3.94
2_1^+	3.61	6.9	104	-24	-0.11	72	0.33	
4_1^+	7.32	0.7	130	-2	0.01	68	0.31	5.35
6_2^+	12.41	8.3	47	-21	0.09	39	0.18	7.29
0_3^+	6.22	0.0	—	—	—	—	—	
2_2^+	6.61	-36	508	124	0.56	160	0.72	4.57
4_2^+	8.11	-52	611	142	0.64	147	0.62	6.05
6_1^+	10.34	-59	611	146	0.66	140	0.63	7.49

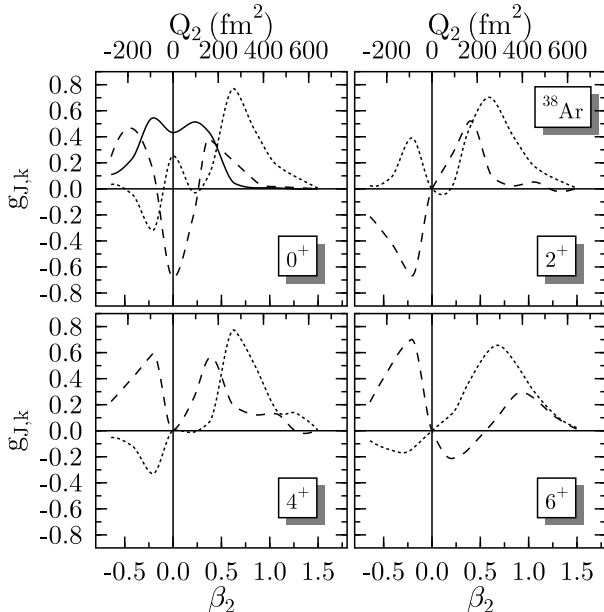


FIG. 9: Collective GCM wave functions $g_{J,k}$ for the lowest spin states of ^{38}Ar . The ground state wave function is drawn with a thick solid line. The wave functions of the ND and SD bands are by dashed and dotted lines, respectively.

in terms of a $\pi[d_{3/2}]_{J=2}^{-2}$ configuration [24, 25]. This assignment is compatible with the pairing gap Δ_p at the proton Fermi surface that we obtain. Indeed, the excitation energy of this two-quasiparticle configuration is approximated in perturbation by $2\Delta_p$, which is equal to 1.96 MeV, rather close to the observed 2.17 MeV.

The MF and PMF energy curves of ^{38}Ar presented in Fig. 7 are very reminiscent of ^{40}Ca . The MF curve exhibits a well-defined spherical minimum. It is considerably softened by angular momentum projection, as shown by the $J = 0$ PMF curve. Moreover, there is a clear in-

TABLE IV: Out-of-band transitions and branching ratios for ^{38}Ar . The k labeling of the state refers to our calculation. Data are taken from [6].

$J_k^+ \rightarrow (J-2)_{k'}^+$	$B(E2; J \rightarrow J-2)$	Branching Ratio		
	($e^2 \text{ fm}^4$)	Calc.	Exp.	
$2_1^+ \rightarrow 0_1^+$	15			
$4_1^+ \rightarrow 2_2^+$	22	14	5 (3)	
$6_2^+ \rightarrow 4_2^+$	126	73	5 (1)	
$2_2^+ \rightarrow 0_1^+$	1			
$2_2^+ \rightarrow 0_2^+$	1			
$4_2^+ \rightarrow 2_1^+$	3	0.5	40 (13)	
$4_2^+ \rightarrow 2_3^+$	34			
$6_1^+ \rightarrow 4_1^+$	110	15	31 (6)	

dication of a shell structure around $\beta_2 = 0.5$. At this deformation, the angular momentum projection on $J = 0$ lowers the energy by approximately 5 MeV, reducing the excitation energy to slightly more than 6 MeV. The GCM results presented in Figs. 8 and 9 are also similar to those obtained for ^{40}Ca : i) an isolated spherical ground state, ii) a set of states which can be grouped into a moderately deformed band (ND band) starting at 3.4 MeV and iii) a SD band with a 6.22 MeV bandhead. Keeping in mind that the present calculation predicts a too small moment of inertia, we estimate that the ND band starts at the correct energy while the SD band is located too high by about 1.8 MeV. These results are comparable in quality to those reported of Ref. [6], which however, in contrast to us, predict slightly too large moments of inertia.

The calculated in-band transition probabilities – which are not yet measured –, the deformation and spectroscopic moments are given in Table III. They confirm the status of the SD band as a rotational band. The

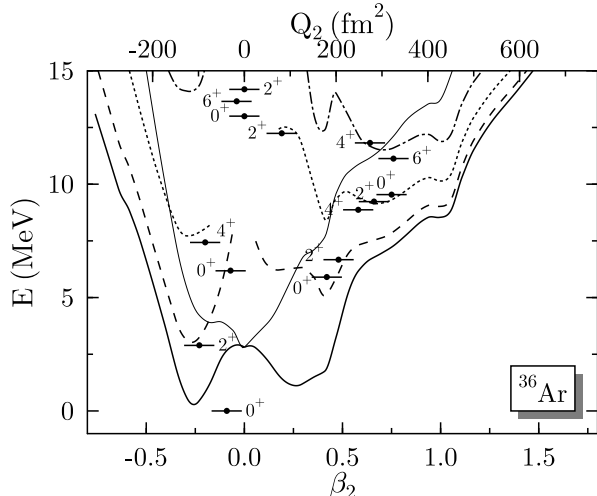


FIG. 10: Same as Fig. 7, but for the nucleus ^{36}Ar .

only existing electromagnetic transition data to be compared with our results concern branching ratios for several states of the two bands. Our results, are given in Table IV.

C. ^{36}Ar

The low-energy spectrum of the $N = Z$ nucleus ^{36}Ar is that of a transitional nucleus. In contrast to ^{40}Ca and ^{38}Ar , a ND band is built directly on the ground state [26]. Recently, a SD band has been observed up to a 16^+ state [4, 5]. The energy of the 0^+ bandhead has been proposed to be at 4.3 MeV. Supporting data can be found in Ref. [27]. In the former references, the data are analyzed with the help of both shell model and cranked Nilsson-Strutinsky calculations. The shell model reproduces the ND band energies very well. Both methods explain the SD band in terms of the promotion of four particles to the p - f shell. According to the diagram of Fig. 2, this excitation is associated with the deformed shell gap at $\beta_2 \approx 0.6$. The calculations indicate that this SD band behaves as a good rotor. They also predict the position of the bandhead to better than 1 MeV. Both theoretical methods reach rather good agreement on $B(E2)$ values. Results of similar quality have been obtained by more schematic projected shell model calculations however with appropriately adjusted parameters [28].

As can be seen in Fig. 10, the MF curve still presents a spherical minimum. It displays neither a secondary minimum nor even a plateau for a deformation close to $\beta_2 = 0.6$. The projection on spin markedly changes the picture. The ground state becomes oblate. At spin 0, the SD shell effect still does not show up as a minimum while higher spin PMF curves present a well-defined minimum which gradually shifts from $\beta_2 = 0.45$ to 0.65. The properties of the GCM states, shown in Figs. 11 and 12, qualitatively reproduce the observed features with one

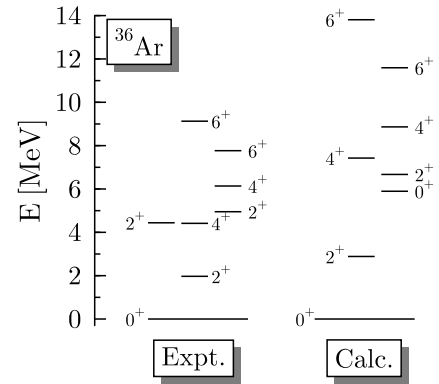


FIG. 11: Same as Fig. 5 for the nucleus ^{36}Ar .

ND and one SD band. Note that the 4.4 MeV, 2^+ level involves a two quasi-particle excitation and is, therefore, not included in our variational space. On the other hand, the SD bandhead energy is predicted too high by about 1.4 MeV and, as for the nuclei studied above, the moments of inertia are too small. In Fig. 12, one sees that the collective wave functions of the SD band are peaked around $\beta_2 \approx 0.55$. This value is larger than that calculated in Ref. [4, 5].

Table V confirms the oblate nature of the ND band, as can be seen from the $g_{0,1}$ wave function and the rotor behavior of the SD band. This feature is not present in the data. From Tables V and VI, one sees that the observed in-band $B(E2)$ values are slightly overestimated, while the out-of-band transition rates are correctly reproduced. Our results show that the inclusion of collective

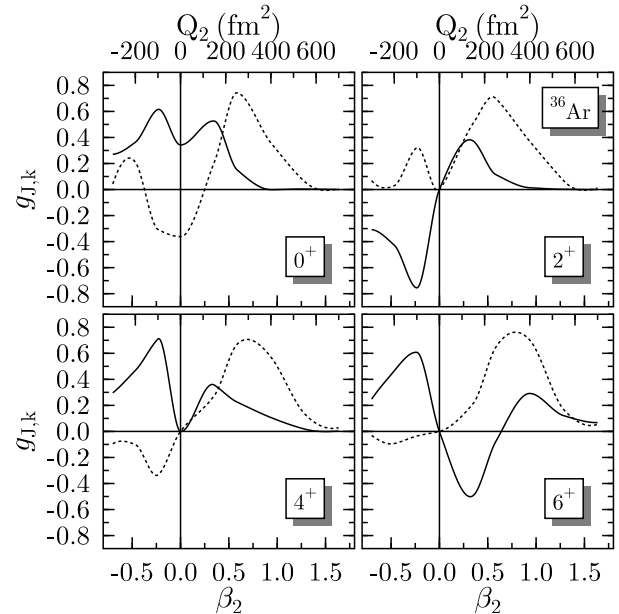


FIG. 12: Collective GCM wave-functions $g_{J,k}$ for low-spin states of ^{36}Ar . The ground-state band and the SD band are drawn with solid and dotted lines respectively.

TABLE V: Energy, spectroscopic moment and transition amplitudes of ground band (upper part) and SD band (lower part) GCM states of ^{36}Ar . The k labeling of the state refers to our calculation. The columns five to eight give the intrinsic moments (see Sect. II B). The last two columns give the experimental excitation energy and $B(E2) \downarrow_{\text{exp}}$ corresponding to the most likely state assignment [4, 5, 29].

GCM State	$E_{J,k}$	Q_c	$B(E2) \downarrow$	$Q_{c2}^{(s)}$	$\beta_{c2}^{(s)}$	$Q_{c2}^{(t)}$	$\beta_{c2}^{(t)}$	E_{exp}	$B(E2) \downarrow_{exp}$
J_k^+	(MeV)	(e fm 2)	(e^2 fm 4)	(e fm 2)		(e fm 2)		(MeV)	(e^2 fm 4)
0_1^+	0.00	0	—	—	—	—	—	0.00	
2_1^+	2.80	13	44	-45	-0.21	47	0.22	1.97	60 ± 6
4_1^+	7.43	12	103	-34	-0.16	60	0.28	4.41	
6_2^+	13.65	-1.3	93	3.3	0.02	55	0.26	9.18	
0_2^+	5.90	0	—	—	—	—	—	4.33	
2_2^+	6.67	-32	366	112	0.52	136	0.63	4.95	
4_2^+	8.87	-48	536	133	0.62	137	0.64	7.76	372 ± 59
6_1^+	11.13	-68	715	171	0.80	151	0.71	9.92	454 ± 67

TABLE VI: Out-of-band transitions in ^{36}Ar . The k labeling of the states refers to our calculation. Data are taken from Refs. [4, 5].

$J_k^+ \rightarrow (J-2)_{k'}^+$	$B(E2) \downarrow (e^2 \text{ fm}^4)$
	Calc. Exp.

quadrupole correlations supports the results obtained by more schematic models such as the cranked Nilsson calculations presented in Refs. [4, 5]

D. ^{32}S

The MF energy curve for the mid-shell, $N = Z$, nucleus ^{32}S , presented in Fig. 13, displays a flat spherical minimum. As can be expected from the single-particle spectrum diagram of Fig. 2, it does not show any structure around $\beta_2 \approx 0.5$. Note that it presents an inflection point at very large deformation, $\beta_2 \approx 1$. In contrast, the $J = 0$ angular momentum projected curve exhibits two well-defined minima at small deformation, the oblate one being the lowest. One also notes a stabilization of the SD minimum which, however, never becomes yrast. These results are similar to those of other mean-field approaches [30, 31, 32, 33]. Note that the authors of [33] suggest that the SD structure may be stabilized at high spin by non-axial octupole deformations.

The GCM calculation leads to the results displayed in Figs. 14 and 15, and the moments and transition rates given in Tables VII and VIII. In agreement with experi-

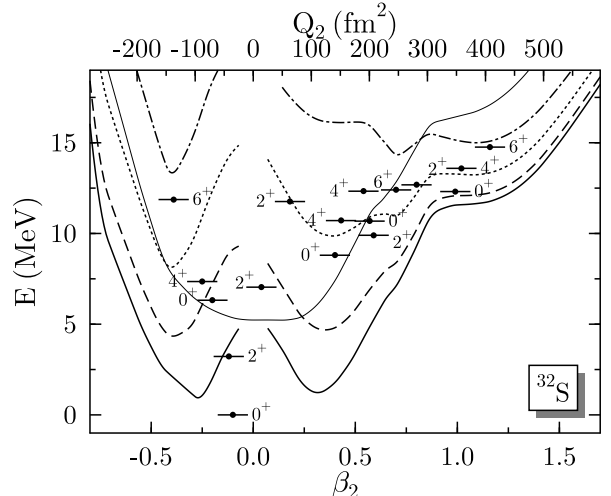


FIG. 13: Same as Fig. 7, but for ^{32}S .

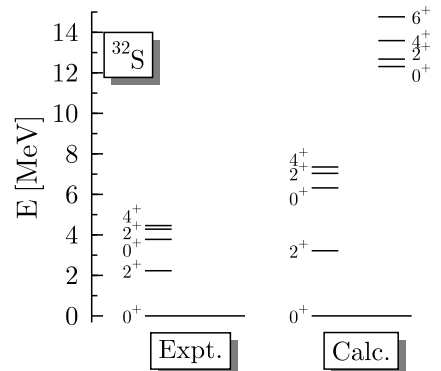


FIG. 14: Same as Fig. 5 for the nucleus ^{32}S .

ment, the levels and energies are those of an anharmonic vibrator with a characteristic 0_1^+ , 2_1^+ and a $(4_1^+, 2_2^+, 0_2^+)$

TABLE VII: Data for the low-lying states in ^{32}S which can be interpreted as anharmonic vibrator states. The k labeling of the states refers to our calculations. Experimental data are taken from [34] and [35].

J_k^+	E (MeV)	Q_s (MeV)	Transition	$B(E2)$ ($e^2 \text{ fm}^4$)	$Q_{c2}^{(s)}$ ($e \text{ fm}^2$)	$Q_{c2}^{(t)}$ ($e \text{ fm}^2$)	E_{exp} (MeV)	$B(E2)_{exp}$ ($e^2 \text{ fm}^4$)
0_1^+	0.00	0.0	—	—	—	—	0.00	—
2_1^+	3.22	2.3	$2_1^+ \rightarrow 0_1^+$	38	2.3	43	2.23	61 ± 3
0_2^+	6.32	—	$0_2^+ \rightarrow 2_1^+$	144	—	12	3.78	72
2_2^+	7.04	-0.7	$2_2^+ \rightarrow 2_1^+$	157	-0.7	74	4.28	54 ± 3
			$2_2^+ \rightarrow 0_1^+$	0.02		0.8		11 ± 2
			$2_2^+ \rightarrow 0_2^+$	2.8		12		
4_1^+	7.35	11.7	$4_1^+ \rightarrow 2_1^+$	94	12	58	4.46	72

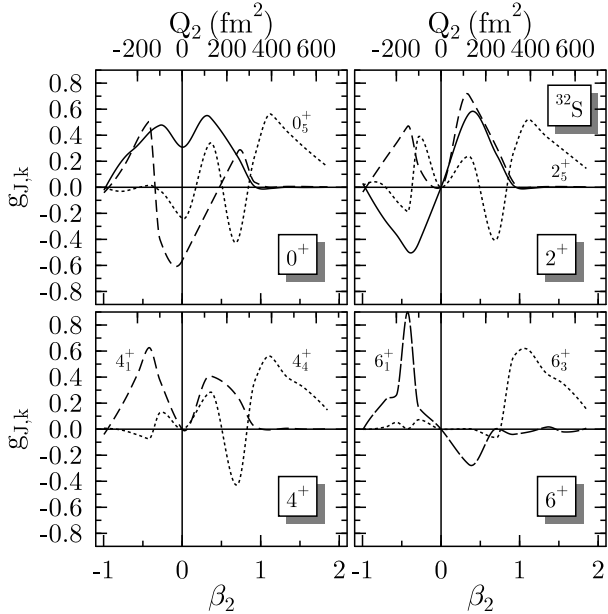


FIG. 15: Collective GCM wave-functions $g_{J,k}$ for the lowest spin states of ^{32}S . The first 0^+ (ground state) and 2^+ are drawn with a thick solid line. The dashed line corresponds to the 0^+ , 2^+ and 4^+ members of the two-phonon triplet, while the SD rotational states are drawn with a dotted lines respectively.

TABLE VIII: Energy, spectroscopic quadrupole moment and $E2$ transition amplitudes of the SD band states of ^{32}S . The k labeling of the state refers to our calculation. The columns five to eight give the intrinsic moments (see Sect. II B).

J_k^+	$E_{J,k}$ (MeV)	Q_c ($e \text{ fm}^2$)	$B(E2) \downarrow$ ($e^2 \text{ fm}^4$)	$Q_{c2}^{(s)}$ ($e \text{ fm}^2$)	$\beta_{c2}^{(s)}$	$Q_{c2}^{(t)}$ ($e \text{ fm}^2$)	$\beta_{c2}^{(t)}$
0_5^+	12.3	0	—	—	—	—	—
2_5^+	12.7	-39	719	136	0.77	190	1.08
4_4^+	13.6	-64	767	176	1.00	164	0.94
6_3^+	14.8	-82	1057	206	1.17	184	1.05

sequence. The vibrational pattern is slightly more prominent in the calculated ratios of $B(E2)$ values than in the observed ones. This may be due to an inaccuracy in the description of the 2_1^+ state which is almost spherical in our calculation while the data suggest a strong prolate deformation. In comparison with similar calculations with the Gogny force [31], the SLy6 force appears to be less performant on this specific point. On the other hand, the overall pattern and, in particular, the triplet of two-phonon states is better described by our calculation.

The GCM predicts a SD band with a large deformation $\beta_2 \approx 0.9$, starting at the high energy of 12 MeV. However, this energy must probably be scaled down, presumably by the same factor than the one that can be deduced from a comparison of experimental and GCM spectra on ^{40}Ca , ^{38}Ar , ^{36}Ar and ^{32}S .

IV. DISCUSSION AND CONCLUSIONS

This article belongs to a series exploring a model starting from a mean-field description of nuclear structure and an effective Hamiltonian valid for the entire nuclear chart. The model attempts a global description of the nuclear ground states and low-energy spectra. Here, the SLy6 Skyrme interaction and a zero-range density dependent pairing force have been used. The building blocks are self-consistent N -body states, based on the HF+BCS method. Extensions in progress involve the Hartree-Fock-Bogoliubov (HFB) method and the cranked HFB method. No assumption is made on the existence of a core and of valence orbitals. The collective basis is generated by a constraint on the intrinsic axial quadrupole moment. This limits the model to even spin and parity collective structures. The symmetries broken at the level of the mean field are restored by means of particle number and angular momentum projection. This transfers the physical description from the intrinsic to the laboratory frame while yielding moments and transitions to be compared directly to experimental data. Finally, the dynamical effects associated with the selected constraint are incorporated by means of a diagonalization of the

initial Hamiltonian within the collective basis (GCM). Other ways to generate collective bases have already been explored by our group (see for instance Ref. [18]), by constraints on monopole, triaxial quadrupole, and octupole deformations or by the construction of a two-quasiparticle excited basis. Essentially, these extensions do not entail a modification of the numerical tools but require more computing time and they have only included the restoration of the particle-number symmetry.

A first test study on the magic nucleus ^{16}O presented in Ref. [8] yielded results demonstrating that the extension of a MF method through restoration of broken symmetries results in a significantly improved description of the level structure and other spectroscopic properties of this nucleus. The present work studies four light nuclides – ^{32}S , ^{36}Ar , ^{38}Ar , ^{40}Ca – to test the model on systems illustrative of a variety of properties encountered in the s - d shell. Another reason to select these nuclei is the recent discovery of superdeformed structures in the three heaviest. Such structures are generally interpreted as resulting from the interaction between s - d and f - p shells.

The results presented in this work are encouraging. The general trends seen for low-lying collective levels are well described both with regard to the relative energy positions within the spectrum of a given isotope and to the evolution from nucleus to nucleus. In particular, as in data, the magic and thus isolated nature of the ground state of ^{40}Ca and ^{38}Ar contrasts with ^{36}Ar and ^{32}S , where the ground state is strongly coupled to other components of the spectrum. Moreover, at small excitation energies, the vibrational features of ^{32}S are well reproduced. Within the same calculational frame, we also find the recently discovered SD structures. We confirm the conclusions drawn from the cranking model and the shell model that the existence of SD bands is connected to a partial occupation of deformation-driving orbitals originating from the $f_{7/2}$ shell. However, in the specific case of ^{40}Ca , a detailed analysis has shown that the association of SD bands with 4p-4h configurations must not be taken too literally. Quadrupole collectivity generating a coherent multi-excitation of p-h configurations of various complexities is probably more representative of the nature of the SD bandhead wave functions. Finally, the $E2$ transition matrix elements of these SD bands agree rather well with the data, indicating that our method correctly reproduces the average quadrupole deformation. We recall that no effective charge is involved in our calculation.

Our calculations display a systematic deficiency in that they predict level densities which are too small. This feature manifests itself through the high excitation energy of the bandheads and the small values of the moments of inertia. At this point, we can only surmise the causes of this problem, as it may be traced either to the model, or to the Hamiltonian, or to both. However, two results seem to exonerate the Hamiltonian, at least as the dominant source of discrepancy. First, the results for the magic nucleus ^{16}O were rather good and, just as in this work, angular momentum projection was shown to lead

to large energy gains by amounts of the order of 5 MeV, reducing by almost an order of magnitude the MF excitation energies of the deformed configurations (see Figs. 3, 7, 10 and 13). Second, similar calculations with another well-tested effective interaction, i.e. the Gogny force, lead to the same phenomenon [31]. In this and earlier references from the same authors, a scaling factor (≈ 0.7) is introduced to compensate for the too low level density. It has been justified on the basis of a comparison between solutions of a cranked mean-field method and a projected method on non-cranked states. In other words, the deficiency does not originate either from the Hamiltonian, nor from the model, but from a too strict limitation of the MF basis. The best description of the (N_0, Z_0) nuclide is obtained by projecting out the (N_0, Z_0) component of the MF solution constrained to have the same mean values of the \hat{N} and \hat{Z} operators. In the same way, the optimal description of a state of spin J should result from the projection of a cranked MF state constrained to have $\langle \hat{J}_x \rangle = J$. These points are also discussed in [36]. One underlying dynamical explanation has to do with the antipairing cranking effect, which increases the moment of inertia as needed to improve our results. In the present work, by projecting out a $J = 6$ component out of a non angular momentum MF solution, we miss the pairing reduction which affects a $\langle \hat{J}_x \rangle = 6$ cranked MF state.

This discussion also delineates possible lines of future developments. On the one hand, in selected cases suggested by experimental data, it may become necessary to enlarge the collective space by taking into account other deformations (as suggested, for instance, by Yamagami and Matsuyanagi [32]). Finally, a promising extension of the present work would involve the projection of angular momentum cranked solutions. Work is presently underway along these three directions.

Acknowledgments

This research was supported in part by the PAI-P5-07 of the Belgian Office for Scientific Policy. We thank R. V. F. Janssens and R. Wyss for fruitful and inspiring discussions. M. B. acknowledges support through a European Community Marie Curie Fellowship.

THE QUADRUPOLE MOMENT IN THE LAB FRAME

In this appendix, we derive the formulas which permits to calculate quadrupole transition matrix elements between symmetry restored mean-field states. Some of the equations given in Ref. [7] contain misprints that are corrected here.

For sake of simple notation, we omit particle-number projection throughout this appendix. It does not alter any of the formulas given here concerning angular momentum. Different from above, we will explicitly in-

clude the angular momentum projection M in the notation. Starting from time-reversal, parity, and axially symmetric (with the z axis as symmetry axis) mean-field states $|q\rangle$ obtained with a constraint on the quadrupole moment labelled as q , projected states $|JMq\rangle$ with total angular momentum J and angular momentum projection M

$$|JMq\rangle = \frac{1}{\mathcal{N}_{Jq}} \hat{P}_{M0}^J |q\rangle, \quad (7)$$

where $\mathcal{N}_{Jq} = \langle q | \hat{P}_{00}^J | q \rangle^{1/2}$ is a normalization factor, are obtained applying the angular-momentum projector [36]

$$\hat{P}_{MK}^J = \frac{2J+1}{8\pi^2} \int d\Omega \mathcal{D}_{MK}^{J*}(\Omega) \hat{R}(\Omega), \quad (8)$$

where $\hat{R}(\Omega) = e^{-i\alpha\hat{J}_z} e^{-i\beta\hat{J}_y} e^{-i\gamma\hat{J}_z}$ is the rotation operator and $\mathcal{D}_{MK}^J(\Omega) = e^{-iM\alpha} d_{MK}^J(\beta) e^{-iK\gamma}$ a Wigner function, which depend both on the Euler angles $\Omega = (\alpha, \beta, \gamma)$, see [37] for details.

The projected GCM states $|JMk\rangle$ are given by

$$|JMk\rangle = \int dq f_{J,k}(q) |JMq\rangle, \quad (9)$$

where the non-orthonormal set of weight functions $f_{J,k}(q)$ is determined variationally by solving the Hill-Wheeler equation. The collective wave functions $g_{J,k}(q)$ given in

figures 4, 9, 12 and 15 above are obtained from the $f_{J,k}(q)$ by a transformation involving the hermitean square root of the norm operator, see [9] and references therein for more details.

The spectroscopic quadrupole moment of the GCM state $|JMk\rangle$ is defined as

$$\begin{aligned} Q_c(J, k) &= \sqrt{\frac{16\pi}{5}} \langle J, M = J, k | \hat{Q}_{20} | J, M = J, k \rangle \\ &= \sqrt{\frac{16\pi}{5}} \int dq \int dq' f_{J,k}^*(q) f_{J,k}(q') \\ &\quad \times \langle J, M = J, k | \hat{Q}_{20} | J, M = J, q' \rangle. \end{aligned} \quad (10)$$

For J and J' integer and even – as assumed here – the matrix element of the projected mean-field states entering Eq. (10) can be expressed in terms of the reduced matrix element $\langle Jq | \hat{Q}_{20} | Jq' \rangle$ [37]

$$\begin{aligned} \langle J, M = J, q | \hat{Q}_{20} | J, M = J, q' \rangle \\ = \frac{\langle J J 20 | J J \rangle}{\sqrt{2J+1}} \langle Jq | \hat{Q}_{20} | Jq' \rangle. \end{aligned} \quad (11)$$

The reduced matrix element involving different values of J appears in the expression of the reduced transition probability between the GCM states k' and k with angular momentum J' and J , respectively

$$\begin{aligned} B(E2, J'_{k'} \rightarrow J_k) &= \frac{e^2}{2J'+1} \sum_{M=-J}^{+J} \sum_{M'=-J'}^{+J'} \sum_{\mu=-2}^{+2} |\langle J M k | \hat{Q}_{2\mu} | J' M' k' \rangle|^2 \\ &= \frac{e^2}{2J'+1} \left| \int dq \int dq' f_{J,k}^*(q) f_{J',k'}(q') \langle Jq | \hat{Q}_2 | J' q' \rangle \right|^2. \end{aligned} \quad (12)$$

The reduced matrix element is evaluated by the commutation of one of the two projection operators in the expression $\hat{P}_{KM}^J \hat{Q}_{2\mu} \hat{P}_{M'K'}^{J'}$ with the quadrupole opera-

tor. After a lengthy, but straightforward application of angular momentum algebra and taking advantage of the symmetries of the mean-field states, one obtains

$$\langle Jq | \hat{Q}_2 | J' q' \rangle = \frac{\sqrt{2J+1} (2J'+1)}{\mathcal{N}_{Jq} \mathcal{N}_{J'q'}} \sum_{\mu=-2}^{+2} \frac{1+(-)^J}{2} \langle J' 02\mu | J \mu' \rangle \int_0^{\pi/2} d\beta \sin(\beta) d_{0\mu}^J(\beta) \langle q | e^{-i\beta\hat{J}_y} \hat{Q}_{2\mu} | q' \rangle \quad (13)$$

where only the “left” states have to be rotated. A similar expression, where only the right states have to be rotated,

is given in [38].

[1] A. M. Nathan and J. J. Kolata, Phys. Rev. C **14**, 171 (1976).

[2] E. Ideguchi, D. G. Sarantites, W. Reviol, A. V. Afanasyev

jev, M. Devlin, C. Baktash, R. V. F. Janssens, D. Rudolph, A. Axelsson, M. P. Carpenter, A. Galindo-Uribarri, D. R. LaFosse, T. Lauritsen, F. Lerma, C. J. Lister, P. Reiter, D. Seweryniak, M. Weiszflog and J. N. Wilson, Phys. Rev. Lett. **87**, 222501 (2001).

[3] C. J. Chiara, E. Ideguchi, M. Devlin, D. R. LaFosse, F. Lerma, W. Reviol, S. K. Ryu, D. G. Sarantites, C. Baktash, A. Galindo-Uribarri, M. P. Carpenter, R. V. F. Janssens, T. Lauritsen, C. J. Lister, P. Reiter, D. Seweryniak, P. Fallon, A. Görgen, A. O. Macchiavelli, and D. Rudolph, Phys. Rev. C **67**, 041303(R) (2003).

[4] C. E. Svensson, E. Caurier, A. O. Macchiavelli, A. Juodagalvis, A. Poves, I. Ragnarsson, S. Åberg, D. E. Appelbe, R. A. E. Austin, C. Baktash, G. C. Ball, M. P. Carpenter, E. Caurier, R. M. Clark, M. Cromaz, M. A. Deleplanque, R. M. Diamond, P. Fallon, M. Furlotti, A. Galindo-Uribarri, R. V. F. Janssens, G. J. Lane, I. Y. Lee, M. Lipoglavsek, F. Nowacki, S. D. Paul, D. C. Radford, D. G. Sarantites, D. Seweryniak, F. S. Stephens, V. Tomov, K. Vetter, D. Ward and C. H. Yu, Phys. Rev. Lett. **85**, 2693 (2000).

[5] C. E. Svensson, A. O. Macchiavelli, A. Juodagalvis, A. Poves, I. Ragnarsson, S. Åberg, D. E. Appelbe, R. A. E. Austin, G. C. Ball, M. P. Carpenter, E. Caurier, R. M. Clark, M. Cromaz, M. A. Deleplanque, R. M. Diamond, P. Fallon, R. V. F. Janssens, G. J. Lane, I. Y. Lee, F. Nowacki, D. G. Sarantites, F. S. Stephens, K. Vetter and D. Ward, Phys. Rev. C **63**, 061301(R) (2001).

[6] D. Rudolph, A. Poves, C. Baktash, R. A. E. Austin, J. Eberth, D. Haslip, D. R. LaFosse, M. Lipoglavsek, S. D. Paul, D. G. Sarantites, C. E. Svensson, H. G. Thomas, J. C. Waddington, W. Weintraub and J. N. Wilson, Phys. Rev. C **65** 034305 (2002).

[7] A. Valor, P.-H. Heenen and P. Bonche, Nucl. Phys. **A671**, 145 (2000).

[8] M. Bender and P.-H. Heenen, Nucl. Phys. **A713**, 39 (2003).

[9] M. Bender, P.-H. Heenen and P.-G. Reinhard, Rev. Mod. Phys. **75**, 121 (2003).

[10] P.-H. Heenen, P. Bonche, J. Dobaczewski, H. Flocard, S. Krieger, J. Meyer, J. Skalski, N. Tajima and M. S. Weiss, Proceedings of the International Workshop on “Nuclear Structure Models”, Oak Ridge, Tennessee, March 16-25, 1992, R. Bengtsson, J. Draayer and W. Nazarewicz (eds.), World Scientific, Singapore, New Jersey, London and Hong Kong, 1992, page 3.

[11] E. Chabanat, P. Bonche, P. Haensel, J. Meyer and R. Schaeffer, Nucl. Phys. **A635** (1998) 231, Nucl. Phys. **A643** (1998) 441(E).

[12] M. Bender, K. Rutz, P.-G. Reinhard and J. A. Maruhn, Eur. Phys. J. **A7**, 467 (2000).

[13] J. Terasaki, P.-H. Heenen, H. Flocard and P. Bonche, Nucl. Phys. **A600**, 371 (1996).

[14] D. L. Hill and J. A. Wheeler, Phys. Rev. **89**, 1102 (1953).

[15] P. Bonche, J. Dobaczewski, H. Flocard, P.-H. Heenen and J. Meyer, Nucl. Phys. **A510** (1990) 466.

[16] K. E. G. Löbner, *Gamma-ray transition probabilities in deformed nuclei*, in W. D. Hamilton [ed.], *The electromagnetic interaction in nuclear spectroscopy*, North-Holland, Amsterdam, Oxford, 1975, page 141.

[17] A. Messiah, *Méchanique Quantique*, Dunod, Paris, 1960.

[18] P.-H. Heenen, A. Valor, M. Bender, P. Bonche and H. Flocard, Eur. Phys. J. **A11**, 393 (2001).

[19] P. Bonche, J. Dobaczewski, H. Flocard and P.-H. Heenen, Nucl. Phys. **A530**, 149 (1991).

[20] W. J. Gerace and A. M. Green, Nucl. Phys. **A93**, 110 (1967); Nucl. Phys. **A123**, 241 (1969).

[21] M. Ulrickson, N. Benczer-Koller, J. R. MacDonald and J. W. Tape, Phys. Rev. C **15**, 186 (1977).

[22] E. Caurier, F. Nowacki, A. Poves and A. Zuker, *The superdeformed excited band of ⁴⁰Ca*, preprint nucl-th/0205036 (2002).

[23] D. C. Zheng, D. Berdichevsky and L. Zamick, Phys. Rev. C **38** (1988) 437.

[24] B. H. Wildenthal and E. Newman, Nucl. Phys. **A118**, 347 (1968).

[25] E. R. Flynn, O. Hansen, R. F. Casten, J. D. Garrett and F. Ajzenberg-Selove, Nucl. Phys. **A246**, 117 (1975).

[26] P. M. Endt, Nucl. Phys. **A521**, 1 (1990).

[27] H. Röpke, J. Brenneisen and M. Lickert, Eur. Phys. J. **A14**, 159 (2002).

[28] G.-L. Long and Y. Sun, Phys. Rev. C **63**, 021305(R) (2001).

[29] S. Raman, C. W. Nestor, Jr. and P. Tikkainen, Atom. Data Nucl. Data Tables **78** (2001) 1.

[30] H. Molique, J. Dobaczewski and J. Dudek, Phys. Rev. C **61**, 044304 (2000).

[31] R. R. Rodriguez-Guzmán, J. L. Egido and L. M. Robledo, Phys. Rev. C **62**, 054308 (2000).

[32] M. Yamagami and K. Matsuyanagi, Nucl. Phys. **A672**, 123 (2000).

[33] T. Tanaka, R. G. Nazmitdinov and K. Iwasawa, Phys. Rev. C **63**, 034309 (2001).

[34] A. Kangasmäki, P. Tikkainen, J. Keinonen, W. E. Ormand, S. Raman, Zs. Fülöp, Á. Z. Kiss and E. Somorjai, Phys. Rev. C **58**, 699 (1998).

[35] M. Babilon, T. Hartmann, P. Mohr, K. Vogt, S. Volz and A. Zilges, Phys. Rev. C **65**, 037303 (2002).

[36] P. Ring and P. Schuck, *The Nuclear Many-Body Problem*, Springer Verlag, New York, Heidelberg, Berlin, 438 (1980).

[37] D. A. Varshalovich, A. N. Moskalev, V. K. Khersonskii, *Quantum Theory of angular momentum*, World Scientific, Singapore, 1988.

[38] R. Rodriguez-Guzmán, J. L. Egido and L. M. Robledo, Nucl. Phys. **A709**, 201 (2002).